Inverse iron oxide/metal catalysts from galvanic replacement

Yifeng Zhu [1,2], Xin Zhang [2], Katherine Koh[1,2], Libor Kovarik[1,3], John L. Fulton[1,2], Kevin M. Rosso[2] & Oliver Y. Gutiérrez [1,2] ✉
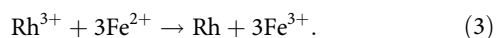
Key chemical transformations require metal and redox sites in proximity at interfaces; however, in traditional oxide-supported materials, this requirement is met only at the perimeters of metal nanoparticles. We report that galvanic replacement can produce inverse FeO_x/metal nanostructures in which the concentration of oxide species adjoining metal domains is maximal. The synthesis involves reductive deposition of rhodium or platinum and oxidation of Fe^{2+} from magnetite (Fe_3O_4). We discovered a parallel dissolution and adsorption of Fe^{2+} onto the metal, yielding inverse FeO_x-coated metal nanoparticles. This nanostructure exhibits the intrinsic activity in selective CO_2 reduction that simple metal nanoparticles have only at interfaces with the support. By enabling a simple way to control the surface functionality of metal particles, our approach is not only scalable but also enables a versatile palette for catalyst design.

[1] Institute for Integrated Catalysis, and Fundamental and Computational Science Directorate, Pacific Northwest National Laboratory, Richland, WA, USA. [2] Physical and Computational Sciences Directorate, Pacific Northwest National Laboratory, Richland, WA, USA. [3] Environmental Molecular Sciences Laboratory, Pacific Northwest National Laboratory, Richland, WA, USA. ✉email: oliver.gutierrez@pnnl.gov

Metal particles play a key role in chemical transformations that require activation of H_2 or hydrogenation/dehydrogenation of substrates. In many cases, the metal particles provide only one step in the catalytic cycle. For instance, metals have low activity in CO_2 reduction because of weak CO_2 adsorption, whereas the polar surface of oxides readily adsorbs CO_2 but suffers from low activity for H_2 activation[1–3]. Thus, metal–oxide interfaces are much more effective because both the redox sites required to activate CO_2 and the metals providing active H_2 are in proximity. Challenges for maximizing such interfaces are stabilizing small metal particles on oxide supports[4–7] or forcing migration of oxides onto metal particles while avoiding harsh synthesis conditions[8–12].

Inverse catalysts—oxides supported on metals—offer an attractive alternative to overcome the constraints of typical supported metal catalysts because reactants can bind to sites in the oxide overlayer, onto the metal domains, or at their interface. Typically, surface science research selects only well-defined inverse catalysts to provide a basic understanding of their adsorption and catalytic properties; however, advancing from this approach into the more complex conditions relevant to technical applications is essential[13–16]. In this regard, a major obstacle is encountered because typical surface science approaches for preparing inverse catalysts, such as reduction at high temperature[12], deposition in ultrahigh vacuum[1,13], and deposition at atomic layers[17], are challenging to scale beyond certain models.

We report here a simple galvanic replacement approach for generating inverse FeO_x/metal nanostructures. During galvanic replacement, one metal dissolves as a sacrificial template while a different metal ion in solution is reductively deposited onto the template. This process is driven by the differences of reduction potentials of the redox pairs, allowing a single, simple, and low-temperature step for synthesis of nanostructures[18–23]. Following this, research has focused on preparing metals[18], metal alloys[19,24], oxides[21], and metal–oxides[25,26] with controllable shapes. In our case, the solid support undergoing oxidation—hyperstoichiometric and sometimes referred to as cation-excess or partially reduced magnetite ($Fe_3O_{3.7}$)[27]—supplies electron equivalents in the form of Fe^{2+} enriched at the oxide surface, which reduce Rh^{3+} or Pt^{4+}, thereby depositing metal nanostructures (Eqs. (1)–(3)).

$$Rh^{3+} + 3e^- \rightarrow Rh. \quad (1)$$

$$Fe^{2+} \rightarrow Fe^{3+} + e^-. \quad (2)$$

$$Rh^{3+} + 3Fe^{2+} \rightarrow Rh + 3Fe^{3+}. \quad (3)$$

We discovered that in addition to acting as sacrificial species, Fe^{2+} dissolves, and adsorbs onto the as-formed metal particles as Fe(II)-oxyhydroxide. The surface property of the metal is thus greatly changed by the FeO_x overlayer, endowing the nanostructure with the high density of active sites for CO_2 reduction that well-dispersed Rh particles have only at the interface with Fe_3O_4. This yields activity and selectivity for CO production significantly higher than well-dispersed Rh particles without FeO_x overlayers. Our method demonstrates that the surface of metal nanoparticles can be manipulated by the sacrificial species during galvanic replacement, whereas galvanic replacement was previously thought to control only nanostructure morphologies.
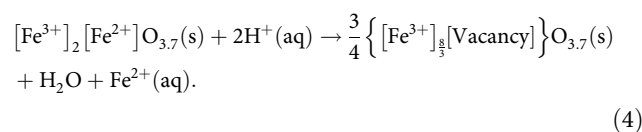
Results and discussion

Identification of FeO_x overlayer on Rh.
We performed the synthesis by simply suspending $Fe_3O_{3.7}$ ("Methods" section and Supplementary Fig. 1 for synthesis) in aqueous $RhCl_3$ solution (Fig. 1a), yielding the as-prepared material (FeO_x/Rh/Fe_3O_4-fresh). High-angle annular dark-field scanning tunneling electron

microscopy (HAADF-STEM) imaging of FeO_x/Rh/Fe_3O_4-fresh (Fig. 1b and Supplementary Figs. 2–5) showed that the deposited nanostructures distribute along the whole surface of Fe_3O_4 with the average size of 6.6 nm. These nanostructures seem to be composed by smaller Rh nanoparticles of around 2 nm. The nanosized structures were further examined by electron energy-loss spectroscopy (EELS) while manipulating the sample to avoid overlapping with the support along z-axis. Maps of Rh $L_{2,3}$ and Fe $L_{2,3}$ edges (Fig. 1b and Supplementary Figs. 3–5) show Fe signals in regions of the Rh domains. The line profile indicates that significant amounts of Fe coincide with Rh particles. The Fe spectra from the Rh domains give a lower loss energy (by 0.7 eV) than the signal from Fe_3O_4 (Supplementary Fig. 3). This indicates that the Fe on Rh nanostructures have a lower average oxidation state (i.e., +2) than that in Fe_3O_4 (+8/3).

Rh K-edge X-ray absorption near edge structure (XANES, Supplementary Fig. 3) showed that the white-line of FeO_x/Rh/Fe_3O_4-fresh is similar to that of Rh foil. Linear combination fitting indicated that 77 mol.% of Rh is metallic (Supplementary Fig. 3 and Supplementary Table 1). This agrees well with the Rh extended X-ray absorption fine-structure (EXAFS) fitting showing that the Rh species have high Rh–Rh coordination (Supplementary Fig. 6 and Supplementary Table 2). The fitting of the spectra required a Rh–O path with a coordination number of 1.9 ± 0.5. Thus, 23 mol.% of Rh remains oxidized, probably because of its interaction with the FeO_x species (Supplementary Table 1). The results indicated that inverse FeO_x/Rh nanostructures were formed where Rh was reductively deposited while Fe(II)-oxyhydroxide species bind onto the Rh.

Mechanism for the formation of FeO_x overlayer.
We used the ferrozine method[28] to monitor changes of Fe^{3+} and Fe^{2+} concentrations during synthesis of FeO_x/Rh/Fe_3O_4-fresh (Fig. 1c). Fe^{2+} was released immediately after $Fe_3O_{3.7}$ was dispersed in the solution of Rh^{3+}, which is consistent with the acidic Fe_3O_4 oxidation chemistry (Eq. (4))[27] because Fe^{2+} is much more soluble than Fe^{3+}, and the solution is initially free of aqueous Fe^{2+} upon first contact the Rh^{3+} solution. The pH was observed to initially drift upwards from ~4 to 5, which is consistent with consumption of protons during the release (see section of methods for pH changes).

$$\left[Fe^{3+}\right]_2\left[Fe^{2+}\right]O_{3.7}(s) + 2H^+(aq) \rightarrow \frac{3}{4}\left\{\left[Fe^{3+}\right]_{\frac{8}{3}}[Vacancy]\right\}O_{3.7}(s) + H_2O + Fe^{2+}(aq). \quad (4)$$

The particle surface will be enriched in Fe^{2+} during the Fe^{2+} release into solution[29], thereby maintaining a dynamic equilibrium[27]. In parallel, Rh^{3+} was reduced and deposited as the nanostructures that adsorb and bind Fe(II)-oxyhydroxide during the progressive Fe^{2+} accumulation on the Fe_3O_4 surface (see below). This leads to a gradual reversal of the reaction in Eq. (4), detectable by a pH decrease from ~5 to 2.5 and an increase in Fe^{3+} in solution, reaching equilibrium after 3 h synthesis time. Note that if Rh^{3+} and Fe^{2+} (Rh^{3+}:Fe^{2+} = 1:3) were mixed at the conditions of the galvanic replacement, neither Rh nor FeO_x particles are observed by HAADF-STEM. Thus, Rh nucleation and growth requires the Fe_3O_4 surface and productions of Fe^{2+} and Fe^{3+} in solution follow different mechanisms.

Because formation of metallic Rh is accompanied by increasing detectable aqueous Fe^{3+} (Eq. (3)) and consumption of Fe^{2+} (Fig. 1c), we attribute the Fe(II)-oxyhydroxide coating on Rh particles to the dynamic equilibrium of the Fe^{2+} release process (i.e., the reverse of Eq. (4))[27,29]. To confirm the selective interaction of Fe^{2+} with Rh, we contacted pre-formed Rh
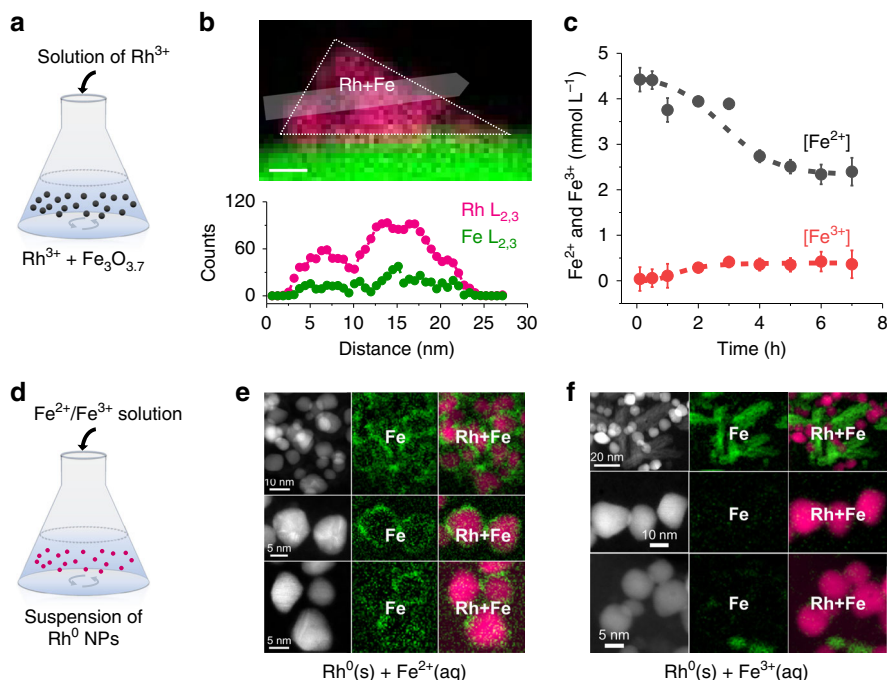
Fig. 1 Synthesis of FeO$_x$/Rh/Fe$_3$O$_4$ by galvanic replacement and reference experiments to elucidate the mechanism of FeO$_x$ coating on Rh. Synthesis of FeO$_x$/Rh/Fe$_3$O$_4$-fresh by galvanic replacement, where powder Fe$_3$O$_{3.7}$ is contacted with a solution containing Rh^{3+} (**a**). Rh and Fe L-edges EELS images of the FeO$_x$/Rh/Fe$_3$O$_4$-fresh and the corresponding line-scan profile showing the FeO$_x$ coating on Rh; the scale bar is 5 nm (**b**); more images can be found in Supplementary Figs. 2–5. Evolution of concentrations of aqueous Fe^{2+} and Fe^{3+} when Fe$_3$O$_{3.7}$ is contacted with the Rh^{3+} solution (**c**). Scheme of the reference experiments, where pre-formed Rh nanoparticles were contacted with solutions containing Fe^{2+} or Fe^{3+} (**d**). HAADF-STEM-EELS images of the solids produced after contacting Rh nanoparticles with Fe^{2+} (**e**) or Fe^{3+} (**f**) in solution showing the selective adsorption of Fe^{2+} on Rh producing the Fe(II)-oxyhydroxide adlayers on Rh.

(a) nRh^{3+} (aq) + $3nFe^{2+}$ (s) → nRh^0 (s) + $3nFe^{3+}$ (aq)

(b) $[Fe^{3+}]_2[Fe^{2+}]O_{3.7}$ (s) + $2H^+$ (aq) → $\frac{3}{4}[Fe^{3+}]_{8/3}[Vacancy]O_{3.7}$ (s) + H_2O + Fe^{2+} (aq)

(c) $(Rh)_n$-OH (s) + Fe^{2+} (aq) → $(Rh)_n$-O-Fe$^+$ (s) + H^+ (aq)
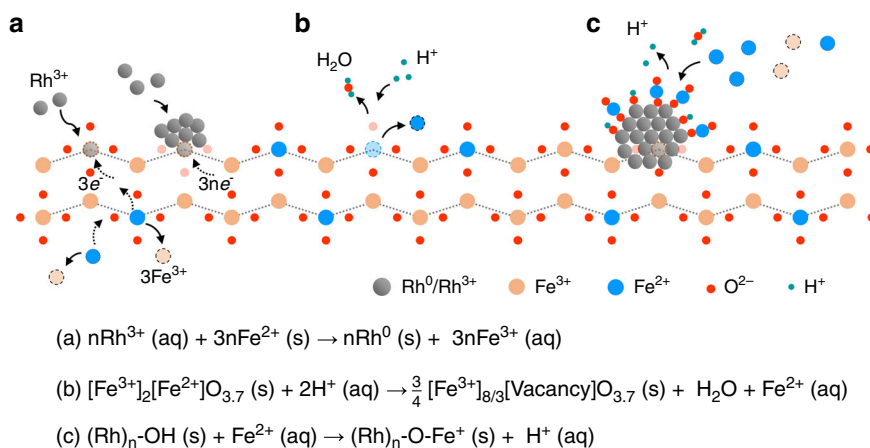
Fig. 2 Mechanism for synthesis of inverse FeO$_x$/Rh/Fe$_3$O$_4$. Formation of Rh nanoparticles on Fe$_3$O$_4$ and release of Fe^{3+} by galvanic replacement (**a**), dissolution of Fe^{2+} species (**b**), and selective deposition of Fe^{2+} on Rh particles (**c**).

nanoparticles with solutions containing either Fe^{2+} or Fe^{3+} cations and analyzed the recovered particles (Fig. 1d). The syntheses of these reference materials are described in the section of methods. The EELS images showed that Fe^{2+} species adsorb on the Rh surface to form a core-shell-like nanostructure (Fig. 1e), whereas Fe^{3+} species precipitate as a segregated phase with only weak association with Rh (Fig. 1f).

Overall, the charge transfer of galvanic replacement consumes Fe^{2+} supplied by Fe$_3$O$_4$ for Rh^{3+} reduction yielding Rh particles (Fig. 2a). In parallel, Fe^{2+} released from the solid (Fig. 2b) adsorbs selectively on Rh (Fig. 2c). In order to

verify the generality of our methodology to prepare inverse nanostructures, we also performed the galvanic replacement between the Pt^{4+} cations and Fe$_3$O$_{3.7}$. The HAADF-STEM-EELS showed that FeO$_x$ species coat the Pt nanoparticles (Supplementary Fig. 7). Hence, during the synthesis of FeO$_x$/metal nanostructures, the Fe^{2+} is not only a sacrificial species as one expects from the galvanic replacement alone, but a key constituent for tuning the surface of the metal nanoparticles. The method offers many possibilities to tune the properties and structures of the final materials by controlling the rates of the individual processes taking place during the synthesis. Further
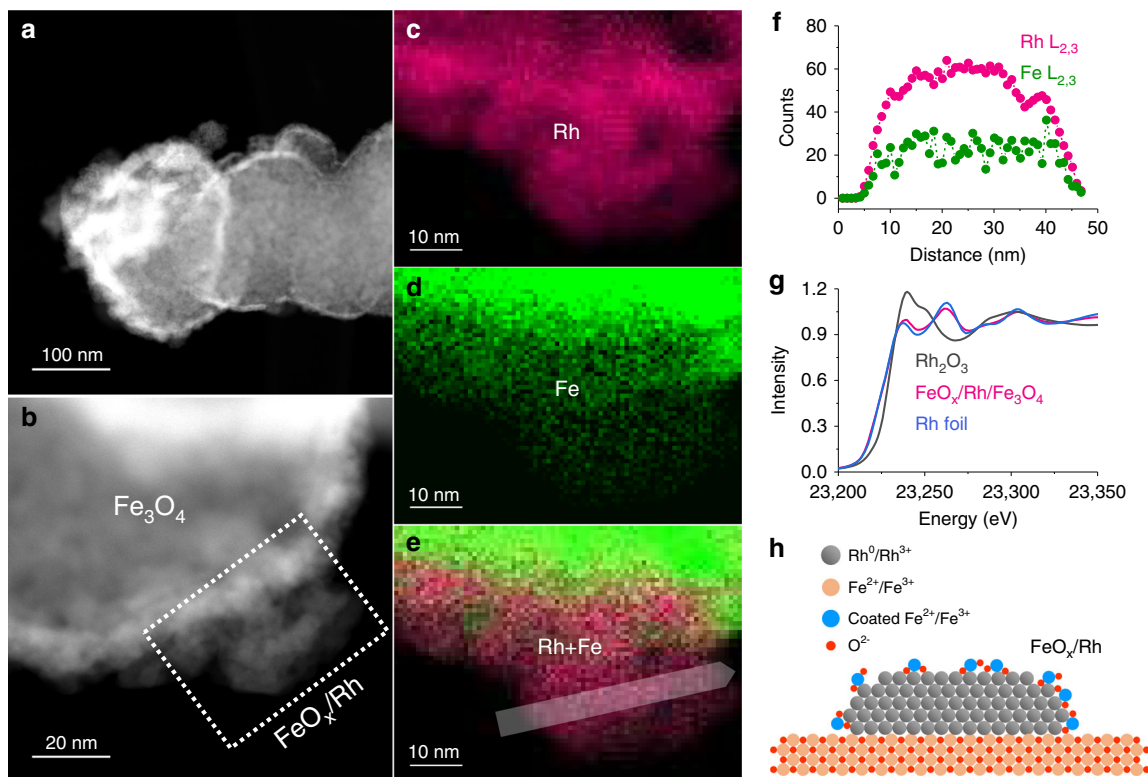
Fig. 3 Structural characterization of FeO$_x$/Rh/Fe$_3$O$_4$ showing the FeO$_x$ coating on Rh. HAADF-STEM-EELS images of FeO$_x$/Rh/Fe$_3$O$_4$ (**a–e**) and the corresponding line profile (**f**) showing mixed FeO$_x$ and Rh domains. Rh K-edge XANES spectra (**g**) of FeO$_x$/Rh/Fe$_3$O$_4$ suggesting Rh is mainly metallic and interacting with FeO$_x$ species. **h** Scheme of the inverse structure on FeO$_x$/Rh/Fe$_3$O$_4$.

work to control the metal particle size and FeO$_x$ coverage is ongoing.

Comparison of FeO$_x$-covered and bare Rh particles supported on Fe$_3$O$_4$. We compared the inverse catalyst with Fe$_3$O$_4$-supported 1–2 nm Rh particles (Rh/Fe$_3$O$_4$) in CO$_2$ hydrogenation. This reference was prepared by precipitating Rh^{3+} on Fe$_3$O$_4$ followed by treatment in air and reduction at 200 °C in H$_2$ (Supplementary Fig. 8 for the Rh particle size distribution). To remove possible adsorbates remaining from synthesis and handling, the FeO$_x$/Rh/Fe$_3$O$_4$-fresh material was treated at the same conditions as Rh/Fe$_3$O$_4$, yielding the material denoted as FeO$_x$/Rh/Fe$_3$O$_4$. This material showed the same features of the parent FeO$_x$/Rh/Fe$_3$O$_4$-fresh. That is, the dispersed FeO$_x$ species still decorated the metallic Rh particles (Fig. 3a–f and Supplementary Fig. 9). The inverse FeO$_x$/Rh nanostructure was unaltered by the heat treatment, in agreement with the lower surface energy of iron oxide (Fig. 3h and Supplementary Table 3), which tends to wet the Rh surface[13].

According to XANES (Fig. 3g) and EXAFS results (Fig. 4a), Rh in both FeO$_x$/Rh/Fe$_3$O$_4$ and Rh/Fe$_3$O$_4$ are mainly metallic with a Rh–Rh distance of 2.68 Å. The Rh–Rh coordination number for FeO$_x$/Rh/Fe$_3$O$_4$ is ~8.9 while for Rh/Fe$_3$O$_4$ it is 6.7 (Supplementary Tables 4 and 5 and Supplementary Figs. 10 and 11). This suggests that the Rh dispersion of FeO$_x$/Rh/Fe$_3$O$_4$ was lower than Rh/Fe$_3$O$_4$ (i.e., 56% and 82%, respectively) (Supplementary Fig. 12). The difference in Rh dispersion was supported by time-of-flight secondary ion mass spectrometry (TOF-SIMS), which showed more abundant Rh$_2$O$^+$ fragments for FeO$_x$/Rh/Fe$_3$O$_4$ than for Rh/Fe$_3$O$_4$ (Supplementary Fig. 13).

In contrast to the EXAFS of FeO$_x$/Rh/Fe$_3$O$_4$ showing 56% Rh dispersion, H$_2$ chemisorption indicates that only 5.6% of Rh is available to adsorb H$_2$ (Fig. 4b and Supplementary Table 6). The

discrepancy between EXAFS and H$_2$ chemisorption is clearly due to the presence of FeO$_x$ overlayer. For Rh/Fe$_3$O$_4$, H$_2$ chemisorption suggests a 70% dispersion, which is in good agreement with EXAFS results (i.e., most of the surface Rh atoms in the nanoparticles are available to adsorb H$_2$). Both FeO$_x$/Rh/Fe$_3$O$_4$ and Rh/Fe$_3$O$_4$ have the same adsorption equilibrium constant for H$_2$ chemisorption (~7, Supplementary Table 6). Therefore, metallic Rh atoms are the sites for H$_2$ activation on both materials.

Catalytic improvement by the FeO$_x$ overlayer. We targeted CO$_2$ hydrogenation to test the activity of our inverse catalysts. Thus, we measured isotherms for CO$_2$ adsorption (Fig. 4c), which showed that FeO$_x$/Rh/Fe$_3$O$_4$ can adsorb more CO$_2$ than Rh/Fe$_3$O$_4$ and pure Fe$_3$O$_4$ (Supplementary Table 6) (i.e., 7.2, 4.3, and 2.2 μmol$_{CO2}$ g^{-1}, respectively, at 33 kPa). The adsorption equilibrium constant for FeO$_x$/Rh/Fe$_3$O$_4$ also is higher than for Rh/Fe$_3$O$_4$ (i.e., 100 and 51, respectively) (Fig. 4c and Supplementary Table 6). Thus, the adsorption sites on the inverse FeO$_x$/Rh catalyst have stronger interactions with CO$_2$ than the sites in Rh/Fe$_3$O$_4$. The differences in adsorption capacity and strength have important consequences in the coverages of molecular species during the reaction (Supplementary Table 7 and Supplementary Figs. 14 and 15), and thus the catalytic performance described below.

The inverse FeO$_x$/Rh/Fe$_3$O$_4$ catalyst showed high activity for CO$_2$ reduction per mol of surface Rh (determined from the Rh–Rh coordination number from EXAFS analysis) compared to that of Rh/Fe$_3$O$_4$ (Fig. 4d). We used this normalization to reflect the surface of the catalysts that is potentially active, i.e., Rh with or without interactions with the support (note however, these trends are the same per mass of catalyst and mass of Rh). The selectivity to CO and the corresponding CO production rates are also higher on FeO$_x$/Rh/Fe$_3$O$_4$ than on Rh/Fe$_3$O$_4$ (Fig. 4e, f). This highlights
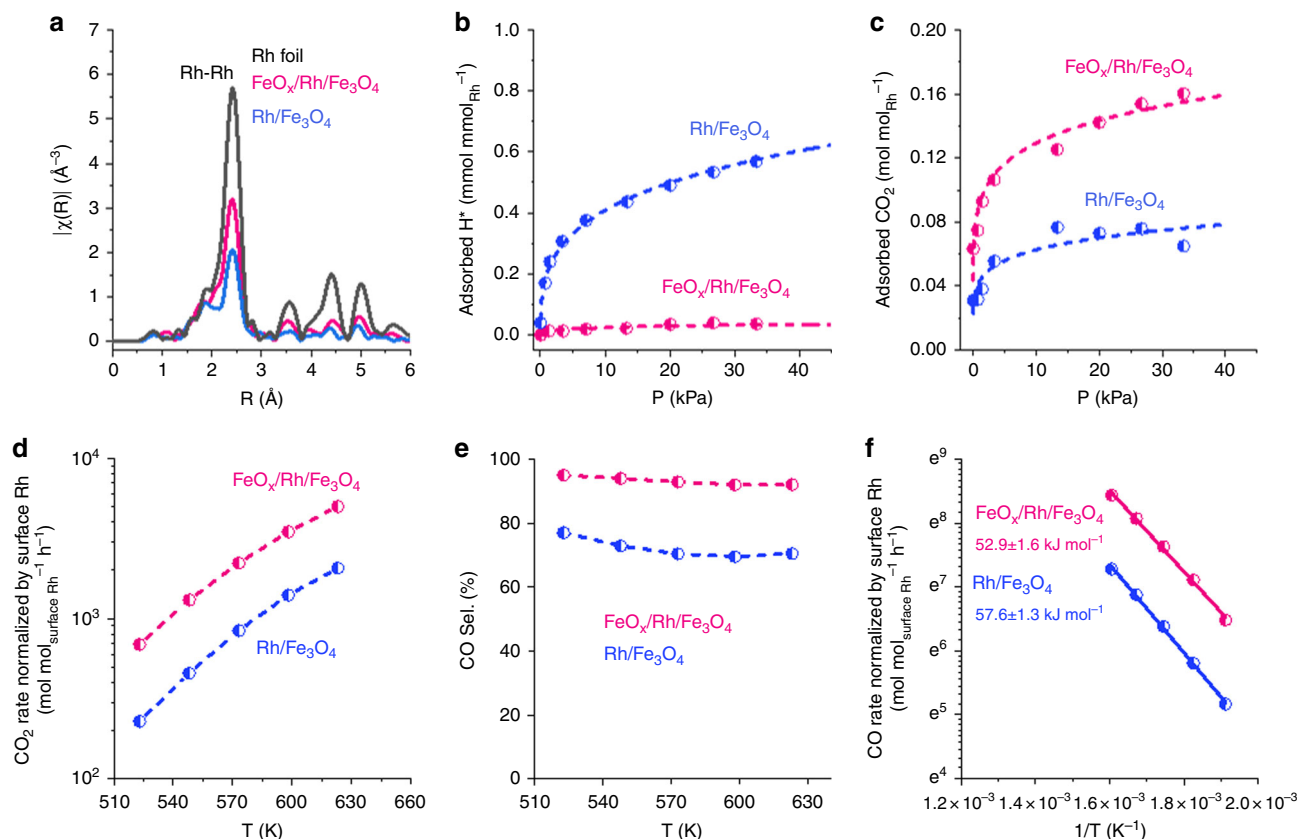
Fig. 4 Characterizations and catalytic performance showing the impact of the FeO$_x$ overlayer on CO$_2$ reduction. Rh K-edge EXAFS spectra (**a**), isotherms of H$_2$ and CO$_2$ chemisorption (**b**, **c**), CO$_2$ conversion rates (**d**), and CO selectivity for CO$_2$ conversion (**e**), and the Arrhenius plots for CO$_2$ reduction to CO (**f**) for FeO$_x$/Rh/Fe$_3$O$_4$ and Rh/Fe$_3$O$_4$. Reaction conditions: 523–623 K, 101 kPa, CO$_2$/H$_2$/He = 7/28/105 mL min^{-1} (gas hourly space velocity of 7 × 10^5 mL g^{-1} h^{-1}). The CO$_2$ and CO rates are normalized to the concentration of surface Rh as derived from EXAFS fitting.

the higher activity of the FeO$_x$-coated particles than simple supported Rh particles. We analyzed the intrinsic activity of the materials not by normalizing rates to the fraction of exposed Rh (as determined from H$_2$ chemisorption) nor to the fraction of Rh covered by oxide species (Supplementary Table 8 and Supplementary Note). Instead, we considered that the uptake of CO$_2$ serves as titration of adsorption sites that can potentially produce CO (see the supporting information for more details). The rates of CO production normalized to the concentration of sites that chemisorb CO$_2$ were, e.g., 1657 and 1222 h^{-1} on FeO$_x$/Rh/Fe$_3$O$_4$ and Rh/Fe$_3$O$_4$, respectively, at 250 °C. The similarity of these values, and of the activation energies for CO production (Fig. 4f), allows us concluding that the highly active and selective sites in both systems are similar. These sites, in view of the negligible activity of SiO$_2$-supported Rh and pure Fe$_3$O$_4$ (Supplementary Table 8) are undoubtedly identified as Rh–Fe$_3$O$_4$ interfaces[30–33].

We also tested the FeO$_x$/Rh nanoparticles (Fig. 1e) and the parent Rh nanoparticles in CO$_2$ reduction (Supplementary Table 9). The FeO$_x$/Rh nanoparticles were one order of magnitude more active than the bare Rh nanoparticles. The bare Rh nanoparticles produced both CO and methane in equimolar concentrations, while FeO$_x$/Rh nanoparticles selectively yielded CO. These observations further support our claim that the FeO$_x$ adlayers increase the activity for CO$_2$ conversion and the selectivity to CO. The FeO$_x$/Rh nanoparticles, however, led to 1–2 orders of magnitude lower rate for CO$_2$ reduction than the inverse FeO$_x$/Rh/Fe$_3$O$_4$ catalyst, which highlights the role of the Fe$_3$O$_4$ support, which maintains the FeO$_x$/Rh nanoparticles separated.

The FeO$_x$/Rh/Fe$_3$O$_4$ inverse catalyst is also more productive than typical supported noble-metal nanoparticles and atomically dispersed Rh (Supplementary Table 10). Thus, leaving some exposed Rh on the surface of FeO$_x$/Rh/Fe$_3$O$_4$ does not lead to low activity because the surface behaves like Rh–Fe$_3$O$_4$ interfaces.

In summary, this galvanic replacement approach to prepare inverse FeO$_x$/metal nanostructures not only yields particularly compelling catalytic reactivity under real conditions but is versatile and easily scalable[13,17,34]. The ability to control the surface functionality of metal nanoparticles enables a palette for catalyst design via galvanic replacement. The presence of the oxide overlayer makes the metal much more efficient for activating CO$_2$ while maintaining its hydrogenation ability. That is, the whole surface of the metal particle functions as metal/oxide interface with redox sites for adsorbing CO$_2$ near metal domains that dissociate H$_2$ but with limited capacity to produce methane.

Methods

Synthesis of FeO$_x$/Rh/Fe$_3$O$_4$-fresh, FeO$_x$/Rh/Fe$_3$O$_4$ and FeO$_x$/Pt/Fe$_3$O$_4$-fresh. The FeO$_x$/Rh/Fe$_3$O$_4$-fresh with the pre-set Rh loading of 0.5 wt% was prepared by galvanic replacement between Rh^{3+} and partially reduced magnetite (Fe$_3$O$_{3.7}$). In a typical procedure, 9.95 g of Fe$_3$O$_4$ was reacted in 5 vol.% H$_2$/N$_2$ at 400 °C in a tube furnace to produce Fe$_3$O$_{3.7}$. The Fe$_3$O$_4$ symmetry group remained for Fe$_3$O$_{3.7}$ after this step (Supplementary Fig. 1). A 10 mL aqueous solution of RhCl$_3$ at a concentration of 5 mg$_{Rh}$ mL^{-1} was mixed with 90 mL deionized water at

room temperature. The $Fe_3O_{3.7}$ was then added to the solution and stirred for 7 h. The resulting material was separated, washed with water, and dried at 80 °C overnight. The as-prepared material was calcined in air at 450 °C with a ramping rate of 2 °C/min. The inductively coupled plasma (ICP) analysis showed that the effective Rh loading in the final material was 0.37 wt%. Prior to the catalytic test, the sample was treated at 200 °C in H_2. The purpose of heat treatments is to remove the possible surface ligands and surface-oxidized Rh species that remained during the synthesis. A material containing Pt ($FeO_x/Pt/Fe_3O_4$-fresh) was prepared by the same method with aqueous solution of H_2PtCl_6 as the precursor and a pre-set Pt loading of 0.5 wt%.

The dynamic changes of the Fe^{2+} and Fe^{3+} concentrations in the aqueous fraction during the galvanic replacement synthesis (for $FeO_x/Rh/Fe_3O_4$-fresh) were analyzed by the ferrozine method[28]. The suspension was centrifuged to isolate the aqueous fraction during the galvanic replacement (0, 0.1, 0.5, 1, 2, 3, 4, 5, 6, and 7 h). The pH values for the aqueous solutions increased slightly at first (from 4.0 to 5.0), and then decreased to ~2.5. The resulting aqueous solutions were diluted in a 10^{-2} M HCl solution and used for the analysis. The Fe^{2+} can react with ferrozine to form a stable magenta complex which gives a maximum absorbance at 562 nm on an ultraviolet–vis spectrophotometer. The Fe^{3+} fraction can be detected by reducing with hydroxylamine hydrochloride solution, stabilized in a buffer, and followed by complexing with ferrozine.

Synthesis of Rh/Fe₃O₄.

The Rh/Fe_3O_4 with a Rh loading of 0.5 wt% was prepared by a urea hydrolysis assisted deposition method. In a typical procedure, 9.95 g of Fe_3O_4 were dispersed in 100 mL deionized water. Then, a 10 mL aqueous solution of $RhCl_3$ at a concentration of 5 mg_{Rh} mL^{-1} was added into the suspension and rigorously stirred for 12 h at room temperature. An excess of urea (urea/[Rh] molar ratio = 60) was added to the suspension for deposition of Rh^{3+}. The Rh^{3+} can be deposited homogeneously and slowly with the help of urea hydrolysis in a hydrothermal condition (90 °C) for 6 h. The resulting material was separated, washed with water, and dried at 80 °C overnight. The as-prepared material was treated in air at 450 °C with a ramping rate of 2 °C min^{-1}. The ICP results suggested that the Rh loading was 0.37 wt%. Prior to the catalytic test, the sample was treated at 200 °C in H_2. A reference Rh/SiO_2 with the Rh loading of 0.5 wt% was also prepared by the urea hydrolysis deposition method, followed by the same treatments before catalytic test.

Synthesis of Rh nanoparticles (PVP method).

In a typical procedure, Rh nanoparticles were synthesized following a polyol-based method. Rh nitrate (Rh amount 100 mg) was dispersed in 60 mL of ethylene glycol in the presence of a stabilizer (PVP) and heated under reflux for 6 h. The Rh nanoparticles then were washed with acetone and water eight times before used for model synthesis experiments.

Mixing of Rh³⁺ and Fe²⁺ cations in solution in the absence of solid.

In a typical procedure, 0.25 mL $RhCl_3$ aqueous solution (5 $mg_{[Rh]}$ mL^{-1}), 1 mL $FeCl_2$ aqueous solution (2 $mg_{[Fe]}$ mL^{-1}), and 4 mL deionized water were mixed at room temperature and stirred for 7 h. This procedures was perfomed in a N_2 glove box.

Reaction of Rh⁰ nanoparticle and Fe²⁺ cations.

After washing three times with deionized water, 1.25 mg Rh^0 nanoparticles were dispersed in 4 mL deionized water and mixed with 1 mL $FeCl_2$ aqueous solution (2 $mg_{[Fe]}$ mL^{-1}) at room temperature. The resulting suspension then was stirred for 7 h. The Rh^0 nanoparticles immersed in Fe^{2+} solution and parent Rh^0 nanoparticles were also diluted in SiO_2 as the reference samples (Rh loading of 0.5%) for handling and catalytic testing.

Reaction of Rh⁰ nanoparticles and Fe³⁺ cations.

After washing three times with deionized, 1.25 mg Rh^0 nanoparticles were dispersed in 4 mL deionized water and mixed with 1 mL $FeCl_3$ aqueous solution (2 $mg_{[Fe]}$ mL^{-1}) at room temperature. The resulting suspension then was stirred for 7 h.

Characterization.

HAADF-STEM measurements were conducted with an aberration-corrected FEI Titan 80-300 STEM operated at 300 kV. EELS mapping and analysis were performed with aberration-corrected JEOL-ARM200F instrument operated at 200 kV. The instrument (Quantum 965) is capable of performing dual EELS experiment. The EELS mapping was performed in the STEM mode in the range of –50 to 500 eV for the zero-loss peak, 300 to 800 eV for the iron signal, and 2500 to 3500 eV for rhodium the signal maps. The zero-loss peak for zero-loss calibration was acquired in low loss spectrum images and aligned at 0 eV. The images and EELS data were analyzed and processed using Gatan Digital Micrograph software. The EELS maps were constructed by analyzing the Fe $L_{2,3}$ (~708 eV), Rh $L_{2,3}$ (~3004 eV), and Pt $M_{4,5}$ (~2122 eV) edge peaks after the background subtraction.

X-ray absorption spectroscopy measurements were conducted in sector 20 of the Advanced Photon Source operated by Argonne National Laboratory. A rejection mirror was used to reduce the effects of harmonics. The metal foil was placed downstream of the sample cell, as a reference to calibrate the photon energy

of each spectrum. The EXAFS spectra were analyzed with the ATHENA (χ(k) oscillation background removal), FEFF9 (theoretical model calculation), and ARTEMIS software packages. The fits to the Rh K-edge EXAFS χ(k) data were weighted by k^2 and windowed between 1.5 Å^{-1} < k < 15.0 Å^{-1} using a Hanning window with dk = 1.0 Å^{-1}.

H_2 and CO_2 chemisorption experiments were conducted with a Micromeritics 2020 instrument. In a typical procedure, 100 to 200 mg of the sample was degassed at 100 °C for 30 min, followed by in situ treatment at 200 °C in H_2 and evacuation at 200 °C for 30 min. Then, the temperature was decreased to 35 °C under vacuum. Prior to the chemisorption experiments, the sample was further evacuated for 40 min. The adsorbates (H_2 or CO_2) were introduced into the system for the measurements of chemisorption isotherms. The first chemisorption isotherm was measured in the pressure range of 0–40 kPa at 35 °C. The sample was evacuated after the first adsorption cycle and a second chemisorption isotherm was recorded. The CO_2 uptake on the parent Fe_3O_4 has been subtracted for plotting and derivation of adsorption parameters.

N_2 physisorption experiments at −196 °C were performed on a Micromeritics 2020 instrument. The samples were degassed in vacuum at 200 °C before the measurements.

TOF-SIMS was applied with a TOF-SIMS V spectrometer (IONTOF GmbH, Münster, Germany) equipped with a 25 keV bismuth cluster ion source, a 20 keV Ar_n^+, and a 2 keV Cs^+/O_2^+ sputtering ion sources. Prior to the TOF-SIMS experiments, the samples were deposited on an Au(111) substrate and exposed to ultrahigh vacuum overnight.

X-ray diffraction experiments were performed in a Philips X′pert Multi-Purpose Diffractometer equipped with a Cu anode (50 kV and 40 mA).

The elemental composition of samples was measured by ICP optical emission spectroscopy (Perkin Elmer 7300DV). Prior to the ICP experiments, the samples were digested in a mixture of $HNO_3/HCl/HF/H_2O$ followed by H_3BO_3 addition for extra HF treatment.

Reaction tests.

The CO_2 reduction was performed in a flow reactor equipped with an online gas chromatograph (Agilent 7890B). In a typical procedure, prior to the catalytic test, 12 mg of 30–80 mesh catalyst (diluted with 50 mg SiC) was loaded into the reactor and treated at 200 °C in 20 vol.% H_2 with a ramping rate of 2 °C min^{-1}. After the reactor reached the target reaction temperature, a mixture of CO_2, H_2, and He with a total flow rate of 140 mL min^{-1} was fed into the reactor (CO_2: H_2:He = 7:28:105).

Correlations of coordination number and metal dispersion.

The correlation between coordination number and metal dispersion was derived from the data in the reference (Supplementary Fig. 12)[35]. The relationship between the coordination number of metal–metal shell and the metal dispersion was derived based on two different shapes of metal particles (spherical and raft-like shapes).

Calculation of adsorption constant and monolayer coverage from isotherms.

The adsorption constant and monolayer coverage were derived from the chemisorption isotherms where chemisorption is treated as a chemical reaction between the gas-phase molecule (A) and the site (*) for adsorption (Eq. (5)).

$$A + {}^* \rightleftarrows A^*. \tag{5}$$

The adsorption can be fitted with a Langmuir adsorption model (Eq. (6)).

$$\theta_A = \frac{V}{V_m} = \frac{KP}{1 + KP}. \tag{6}$$

The adsorption parameters can be obtained from the linear form of Eq. (2) (Eq. (7)). In Eq. (7), θ_A is the fractional coverage of the adsorption sites, P is the partial pressure of the adsorbate, V_m is the volume of the monolayer, and K is the equilibrium adsorption constant.

$$\frac{1}{\theta_A} = V_m\left(\frac{1}{V}\right) = \frac{1}{K}\left(\frac{1}{P}\right) + 1. \tag{7}$$

Data availability

The source data underlying Figs. 1–4 are provided as a Source Data file. The other relevant data that support the findings of this study are available from the corresponding author upon request. Source Data are provided with this paper.

References

1. Graciani, J. et al. Highly active copper-ceria and copper-ceria-titania catalysts for methanol synthesis from CO_2. *Science* **345**, 546–550 (2014).

2. Kattel, S., Liu, P. & Chen, J. G. Tuning selectivity of CO_2 hydrogenation reactions at the metal/oxide interface. *J. Am. Chem. Soc.* **139**, 9739–9754 (2017).
3. Kattel, S., Ramírez, P. J., Chen, J. G., Rodriguez, J. A. & Liu, P. Active sites for CO_2 hydrogenation to methanol on Cu/ZnO catalysts. *Science* **355**, 1296–1299 (2017).
4. Holewinski, A., Idrobo, J.-C. & Linic, S. High-performance Ag–Co alloy catalysts for electrochemical oxygen reduction. *Nat. Chem.* **6**, 828 (2014).
5. Calle-Vallejo, F. et al. Finding optimal surface sites on heterogeneous catalysts by counting nearest neighbors. *Science* **350**, 185–189 (2015).
6. Matsubu, J. C., Yang, V. N. & Christopher, P. Isolated metal active site concentration and stability control catalytic CO_2 reduction selectivity. *J. Am. Chem. Soc.* **137**, 3076–3084 (2015).
7. Zhao, M. et al. Ru octahedral nanocrystals with a face-centered cubic structure, {111} facets, thermal stability up to 400 °C, and enhanced catalytic activity. *J. Am. Chem. Soc.* **141**, 7028–7036 (2019).
8. Tauster, S. J., Fung, S. C. & Garten, R. L. Strong metal-support interactions. Group 8 noble metals supported on titanium dioxide. *J. Am. Chem. Soc.* **100**, 170–175 (1978).
9. Haller, G. L. & Resasco, D. E. Metal–support interaction: group VIII metals and reducible oxides. In Eley, D. D., Pines, H. & Weisz P. B. (eds) *Advances in Catalysis.* (Academic Press, 1989).
10. Dulub, O., Hebenstreit, W. & Diebold, U. Imaging cluster surfaces with atomic resolution: the strong metal-support interaction state of Pt supported on $TiO_2(110)$. *Phys. Rev. Lett.* **84**, 3646–3649 (2000).
11. Tang, H. et al. Ultrastable hydroxyapatite/titanium-dioxide-supported gold nanocatalyst with strong metal–support interaction for carbon monoxide oxidation. *Angew. Chem. Int. Ed.* **55**, 10606–10611 (2016).
12. Matsubu, J. C. et al. Adsorbate-mediated strong metal-support interactions in oxide-supported Rh catalysts. *Nat. Chem.* **9**, 120–127 (2017).
13. Fu, Q. et al. Interface-confined ferrous centers for catalytic oxidation. *Science* **328**, 1141–1144 (2010).
14. Senanayake, S. D., Stacchiola, D. & Rodriguez, J. A. Unique properties of ceria nanoparticles supported on metals: novel inverse ceria/copper catalysts for CO oxidation and the water-gas shift reaction. *Acc. Chem. Res.* **46**, 1702–1711 (2013).
15. Rodriguez, J. A. et al. Inverse oxide/metal catalysts in fundamental studies and practical applications: a perspective of recent developments. *J. Phys. Chem. Lett.* **7**, 2627–2639 (2016).
16. Zhang, J. & Medlin, J. W. Catalyst design using an inverse strategy: from mechanistic studies on inverted model catalysts to applications of oxide-coated metal nanoparticles. *Surf. Sci. Rep.* **73**, 117–152 (2018).
17. Cao, L. et al. Atomically dispersed iron hydroxide anchored on Pt for preferential oxidation of CO in H_2. *Nature* **565**, 631–635 (2019).
18. Sun, Y. & Xia, Y. Shape-controlled synthesis of gold and silver nanoparticles. *Science* **298**, 2176–2179 (2002).
19. Zhang, H., Watanabe, T., Okumura, M., Haruta, M. & Toshima, N. Catalytically highly active top gold atom on palladium nanocluster. *Nat. Mater.* **11**, 49–52 (2012).
20. Xia, X., Wang, Y., Ruditskiy, A. & Xia, Y. Galvanic replacement: a simple and versatile route to hollow nanostructures with tunable and well-controlled properties. *Adv. Mater.* **25**, 6313–6333 (2013).
21. Oh, M. H. et al. Galvanic replacement reactions in metal oxide nanocrystals. *Science* **340**, 964–968 (2013).
22. An, K. & Hyeon, T. Synthesis and biomedical applications of hollow nanostructures. *Nano Today* **4**, 359–373 (2009).
23. Cobley, C. M. & Xia, Y. Engineering the properties of metal nanostructures via galvanic replacement reactions. *Mater. Sci. Eng. R. Rep.* **70**, 44–62 (2010).
24. González, E., Arbiol, J. & Puntes, V. F. Carving at the nanoscale: sequential galvanic exchange and kirkendall growth at room temperature. *Science* **334**, 1377–1380 (2011).
25. Kim, K. W., Kim, S. M., Choi, S., Kim, J. & Lee, I. S. Electroless Pt deposition on Mn_3O_4 nanoparticles via the galvanic replacement process: electrocatalytic nanocomposite with enhanced performance for oxygen reduction reaction. *ACS Nano* **6**, 5122–5129 (2012).
26. Sinatra, L. et al. A Au/Cu_2O–TiO_2 system for photo-catalytic hydrogen production. A pn-junction effect or a simple case of in situ reduction? *J. Catal.* **322**, 109–117 (2015).
27. Peng, H. et al. Reversible Fe(ii) uptake/release by magnetite nanoparticles. *Environ. Sci* **5**, 1545–1555 (2018).
28. Viollier, E., Inglett, P. W., Hunter, K., Roychoudhury, A. N. & Van Cappellen, P. The ferrozine method revisited: Fe(II)/Fe(III) determination in natural waters. *Appl Geochem.* **15**, 785–790 (2000).
29. Pearce, C. I. et al. Synthesis and properties of titanomagnetite ($Fe_{3-x}Ti_xO_4$) nanoparticles: a tunable solid-state Fe(II/III) redox system. *J. Colloid Interface Sci.* **387**, 24–38 (2012).
30. Hakeem, A. A. et al. The role of rhodium in the mechanism of the water–gas shift over zirconia supported iron oxide. *J. Catal.* **313**, 34–45 (2014).
31. Amoyal, M., Vidruk-Nehemya, R., Landau, M. V. & Herskowitz, M. Effect of potassium on the active phases of Fe catalysts for carbon dioxide conversion to liquid fuels through hydrogenation. *J. Catal.* **348**, 29–39 (2017).
32. Utsis, N., Landau, M. V., Erenburg, A., Nehemya, R. V. & Herskowitz, M. Performance of reverse water gas shift on coprecipitated and C-templated BaFe-hexaaluminate: the effect of Fe loading, texture, and promotion with K. *ChemCatChem* **10**, 3795–3805 (2018).
33. Chou, C.-Y., Loiland, J. A. & Lobo, R. F. Reverse water-gas shift iron catalyst derived from magnetite. *Catalysts* **9**, 773 (2019).
34. Chen, G. et al. Interfacial effects in iron-nickel hydroxide–platinum nanoparticles enhance catalytic oxidation. *Science* **344**, 495–499 (2014).
35. Kip, B. J., Duivenvoorden, F. B. M., Koningsberger, D. C. & Prins, R. Determination of metal particle size of highly dispersed Rh, Ir, and Pt catalysts by hydrogen chemisorption and EXAFS. *J. Catal.* **105**, 26–38 (1987).

Author contributions

Y.Z. and O.Y.G. led the project and conceived the experiments. Y.Z., X.Z., and K.K. performed the material synthesis. L.K. was responsible for the microscopy studies. J.L.F. was responsible for the X-ray absorption spectroscopy studies. K.M.R. contributed to the analysis of the mechanism and manuscript writing. Y.Z. and O.Y.G. wrote the manuscript with the inputs from all authors.

Competing interests

The authors declare no competing interests.

Additional information

Supplementary information is available for this paper at https://doi.org/10.1038/s41467-020-16830-4.

Correspondence and requests for materials should be addressed to O.Y.Gér.

Peer review information *Nature Communications* thanks Miron Landau and other, anonymous, reviewers for their contributions to the peer review of this work.

Reprints and permission information is available at http://www.nature.com/reprints

Publisher's note Springer Nature remains neutral with regard to jurisdictional claims in published maps and institutional affiliations.